Behavioral/Systems/Cognitive

Phase–Amplitude Coupling in Human Electrocorticography Is Spatially Distributed and Phase Diverse

Roemer van der Meij,[1] **Michael Kahana,**[2] **and Eric Maris**[1]

[1]Radboud University Nijmegen, Donders Institute for Brain Cognition and Behaviour, 6525 HR, Nijmegen, and [2]Department of Psychology, University of Pennsylvania, Philadelphia, Pennsylvania 19104

Spatially distributed phase-amplitude coupling (PAC) is a possible mechanism for selectively routing information through neuronal networks. If so, two key properties determine its selectivity and flexibility, phase diversity over space, and frequency diversity. To investigate these issues, we analyzed 42 human electrocorticographic recordings from 27 patients performing a working memory task. We demonstrate that (1) spatially distributed PAC occurred at distances >10 cm, (2) involved diverse preferred coupling phases, and (3) involved diverse frequencies. Using a novel technique [*N*-way decomposition based on the PARAFAC (for Parallel Factor analysis) model], we demonstrate that (4) these diverse phases originated mainly from the phase-providing oscillations. With these properties, PAC can be the backbone of a mechanism that is able to separate spatially distributed networks operating in parallel.

Introduction

In a fast-changing complex environment, it is essential that the brain can selectively route information through multiple networks operating in parallel. Oscillatory coupling provides the temporal and spatial dynamics necessary to implement this. Oscillations reflect rhythmic modulations of neuronal excitability, affecting the efficacy of incoming EPSPs and the probability of spike output. It has been proposed that coherently oscillating networks create selective windows of communication between neuronal groups by synchronizing their periods of maximum excitability (Fries, 2005). We investigated spatially distributed phase-amplitude coupling (PAC), a phenomenon that may emerge in spatially distributed oscillating networks. We observed two key properties, phase diversity and frequency diversity, that allow spatially distributed PAC to flexibly and selectively route information through distributed neuronal networks.

PAC describes the coupling between the phase of a slow oscillation and the amplitude of a fast oscillation, with the highest amplitude occurring at the so-called preferred coupling phase (Jensen and Colgin, 2007; Lakatos et al., 2008; Canolty and Knight, 2010). PAC has been observed in multiple species, including rats (Chrobak and Buzsáki, 1998; Sirota et al., 2008; Tort et al., 2008), monkeys (Lakatos et al., 2005, 2008), and humans (Schack et al., 2002; Bruns and Eckhorn, 2004; Mormann et al., 2005; Canolty et al., 2006; Cohen, 2008; Osipova et al., 2008; Miller et al., 2010; Voytek et al., 2010; Maris et al., 2011). A recent study has shown that PAC in human electrocorticography (ECoG) is widely spatially distributed (Maris et al., 2011), which is a key requirement for routing information through distributed networks. Using a novel decomposition technique, this study showed that amplitude- and phase-providing oscillations occurred at broadly distributed sites. However, the decomposition only allowed for diversity over space in the preferred coupling phases of the amplitude-providing oscillations and not of the phase-providing oscillations. Selective routing of information could greatly benefit from phase diversity in the phase-providing oscillation, because its phase could be used to select neuronal populations for interactions. Such phase diversity has not been shown so far. Frequency diversity is another key property determining the flexibility of PAC in selective routing of information. Although theta–gamma PAC dominates the literature, recent reports (He et al., 2010; Miller et al., 2010; Maris et al., 2011) have shown that PAC occurs at many different frequencies.

We analyzed ECoG recordings from 27 patients to investigate the phase diversity and frequency diversity in spatially distributed PAC. We show that PAC occurred over distances that exceed 10 cm, that there was strong phase diversity, and that it involved diverse frequencies. Using a modified version of *N*-way decomposition based on the PARAFAC (for Parallel Factor analysis) model (Maris et al., 2011), we were able to show that spatially distributed phase-providing oscillations were the main source of phase diversity. These oscillations showed large and consistent phase diversity over space. In contrast, the amplitude-providing oscillations showed bursts that were much more synchronized. This phase and frequency diversity are two important attributes that determine how flexibly and selectively spatially distributed PAC can route information through distributed networks operating in parallel.

Materials and Methods

Subjects. Twenty-seven patients (12 female, 15 male) with pharmacoresistant epilepsy were implanted with subdural grid, strip, and depth electrodes before resective surgery. Patients were selected from a large

Received Sept. 21, 2011; revised Oct. 17, 2011; accepted Oct. 24, 2011.

Author contributions: R.v.d.M. and E.M. designed research; R.v.d.M. performed research; M.K. contributed unpublished reagents/analytic tools; R.v.d.M. analyzed data; R.v.d.M. and E.M. wrote the paper.

We gratefully acknowledge the support of the BrainGain Smart Mix Programme of the Dutch Ministry of Economic Affairs and the Dutch Ministry of Education, Culture, and Science.

The authors declare no competing financial interests.

Correspondence should be addressed to Eric Maris, Radboud University Nijmegen, Donders Institute for Brain Cognition and Behaviour, 6525 HR Nijmegen, The Netherlands. E-mail: e.maris@donders.ru.nl.

DOI:10.1523/JNEUROSCI.4816-11.2012

 0270-6474/12/320111-13$15.00/0;

pool of datasets if they had >15 electrodes and >70 trials per recording session after artifact rejection. Informed consent was obtained from the patients or their guardians if they were underage. The research protocol was approved by the appropriate institutional review boards at the Hospital at the University of Pennsylvania (Philadelphia, PA), Children's Hospital (Philadelphia, PA), University Clinic (Freiburg, Germany), Children's Hospital (Boston, MA), and Brigham and Women's Hospital (Boston, MA). Some of the datasets have been analyzed previously, but the analyses presented here are novel (Rizzuto et al., 2003; Raghavachari et al., 2006; Jacobs and Kahana, 2009; van Vugt et al., 2010) or complementary (Maris et al., 2011).

Experimental paradigm. Recordings were obtained from patients performing a Sternberg working memory task (Sternberg, 1966). Patients were presented with a series of letters (from one to six) on a computer screen that they had to remember. At the beginning of each trial, a fixation cross was presented, followed by 700 ms of letter presentation, and then by 275–350 ms (uniformly distributed) of blank screen. The last letter was followed by a retention interval of 425–575 ms (uniformly distributed), after which a probe letter was presented. Patients had to indicate by key press whether the probe letter was part of the previous letter series. After the key press, visual feedback was given and the patient could initiate the next trial by another key press. The main purpose of our study was to characterize fundamental properties of PAC (spatial distribution, phase diversity, and frequency diversity), and therefore we did not investigate any behavioral contrasts (e.g., correct vs incorrect) or stimulus type contrasts (e.g., number of letters). We only analyzed the period between the fixation cross and the onset of the probe letter, during which patients were actively engaged.

Recordings and preprocessing. Electrophysiological recordings were obtained from subdural grid, strip, and depth electrodes. Recordings were sampled at 256–1024 Hz, depending on the hospital, and were referenced to a common average reference. Note that using a nearest-neighbor bipolar referencing scheme did not substantially change the electrode pairs that showed strong PAC or the level of diversity in the preferred coupling phases. Only recordings from grid and strip electrodes were analyzed. Artifact rejection was performed by visual inspection. All trials and/or electrodes contaminated by epileptiform activity were removed. To remove power line noise, we band-stop filtered the data with 1 Hz windows at 50 and 60 Hz (depending on continent) and at other frequencies containing line noise. All recordings were bandpass filtered between 0.01 and 100 Hz. All filters were fourth-order Butterworth.

Electrode locations were determined by first coregistering a postoperative computed tomography scan with a higher-resolution preoperative magnetic resonance image. All patients' brains were normalized to Talairach space (Talairach and Tornoux, 1988), and coordinates were subsequently computed. All preprocessing and the first step of our spectral analyses were performed using the FieldTrip open-source MATLAB toolbox (Oostenveld et al., 2011) developed at the Donders Institute for Brain, Cognition, and Behavior (http://www.ru.nl/neuroimaging/fieldtrip).

Amplitude-weighted phase-locking factor. To quantify PAC, we calculated amplitude-weighted phase-locking factors (wPLFs). These coefficients were calculated using the output of a time-resolved spectral analysis. This spectral analysis was performed by convolving the data with complex-valued wavelets, one for every frequency of interest. All wavelets were obtained from an element-wise multiplication of a three-cycle complex exponential and a Hanning taper of equal length. For every given sampling rate, we only used frequencies for which the corresponding wavelet has an integer number of samples per cycle. Under this constraint, we selected frequencies between 2 and 67 Hz in steps of ~1 Hz. This resulted in one complex-valued time series per trial per frequency bin, called the wavelet transform, describing the time-varying amplitudes and phases.

A wPLF is a complex-valued number representing the relation averaged over time between the phase of one oscillation (obtained from electrode k at frequency m) and the amplitude of another (obtained from electrode j at frequency l). Thus, a wPLF is indexed by an electrode pair (indices k and j) and a frequency pair (indices m and l). A wPLF is normalized, with magnitude ranging from 0 to 1. The magnitude of a wPLF measures the consistency, over trials, of the phase of the phase-providing oscillation at which amplitude increases of the amplitude-providing oscillations occur. The angle of a wPLF indicates this phase, called the preferred coupling phase. A wPLF is amplitude weighted because trials with high amplitudes in one oscillation have a bigger influence than trials with low amplitudes.

The calculation of the wPLFs can be expressed as follows:

$$\mathrm{wPLF}_{jklm} = \frac{\langle A(x_j, f_l),\, W(x_k, f_m)\rangle}{\|A(x_j, f_l)\| \cdot \|W(x_k, f_m)\|}, \qquad (1)$$

in which $A(x_j, f_l)$ denotes the mean-centered absolute-value of the wavelet transform at frequency l of the raw signal x of electrode j, $W(x_k, f_m)$ denotes the wavelet transform at frequency m of the raw signal x of electrode k, $\langle\ ,\ \rangle$ denotes the inner product, and $\|\ \|$ denotes the norm. wPLFs were computed for all possible electrode and frequency pairs. Thus, each electrode in the dataset provides amplitude and phase information for PAC with all other electrodes and for all estimated frequencies. This results in one 4-way array of wPLFs for each dataset. The dimensions correspond to (1) amplitude-providing electrodes (of size J), (2) phase-providing electrodes (of size K), (3) amplitude-providing frequencies (of size L), and (4) phase-providing frequencies (of size M). We show a schematic of the construction of this 4-way array in Figure 1, *A* and *B*.

Selecting significant wPLFs. As a part of the analysis of the 4-way arrays of wPLFs, statistically significant wPLFs were selected. Statistical significance was assessed by comparing every wPLF to a dataset-specific reference distribution obtained under the null hypothesis that the time-varying amplitudes and phases are uncorrelated. Reference distributions were created by randomly pairing the amplitudes of one trial with the phases of another trial. This was repeated 50 times for each dataset, providing 50 random wPLFs for each electrode pair and frequency pair. A normal probability density function was then estimated for every wPLF, using the mean and SD of the magnitude of these 50 random wPLFs. wPLFs were selected if their magnitude surpassed the 99th percentile of this estimated probability density function. Apart from this selection based on a statistical threshold, we also removed all wPLFs in which the phase-providing frequency is higher than or equal to the amplitude-providing frequency.

Evaluating the reliability of preferred coupling phases. To evaluate the reliability of the preferred coupling phase of our significant wPLFs, we used a split-half procedure. This involved a random split of the trials of each dataset in two partitions, followed by constructing a 4-way array of wPLFs for both partitions. In this way, we obtained two independent estimates of every wPLF. The more the preferred coupling phase is influenced by random noise, the larger the phase difference will be between the two estimates. Based on these split-half wPLFs, we calculated a split-half reliability coefficient:

$$\text{splilt-half reliability} = \left| \frac{1}{J} \sum_{j=1}^{J} e^{i(\theta_{1j} - \theta_{2j})} \right|. \qquad (2)$$

In this formula, we first take the difference between the preferred coupling phase of the wPLFs of the first partition θ_{1j} and of the second partition θ_{2j}. We do this for all J significant wPLFs, as determined above (using the 4-way array of wPLFs based on all trials). These phase differences are then expressed as unit-magnitude complex numbers and averaged over all significant wPLFs (indexed by j). The split-half reliability coefficient is then attained by taking the absolute value of the resulting complex number, also known as the mean resultant vector of phase differences. Such a coefficient was calculated for each dataset.

N-way decomposition based on the PARAFAC model. We use *N*-way decomposition to refer to the decomposition of an *N*-way array with more than two dimensions. Unlike 2-way decompositions, such as principal and independent component analysis, *N*-way decomposition has not been used extensively in neuroscience (for exceptions, see Beckmann and Smith, 2005; Mørup et al., 2006). *N*-way decomposition decomposes an *N*-way array into several components, each consisting of *N* loading vectors, one corresponding to each dimension of the original array. Every component describes one aspect of the array,

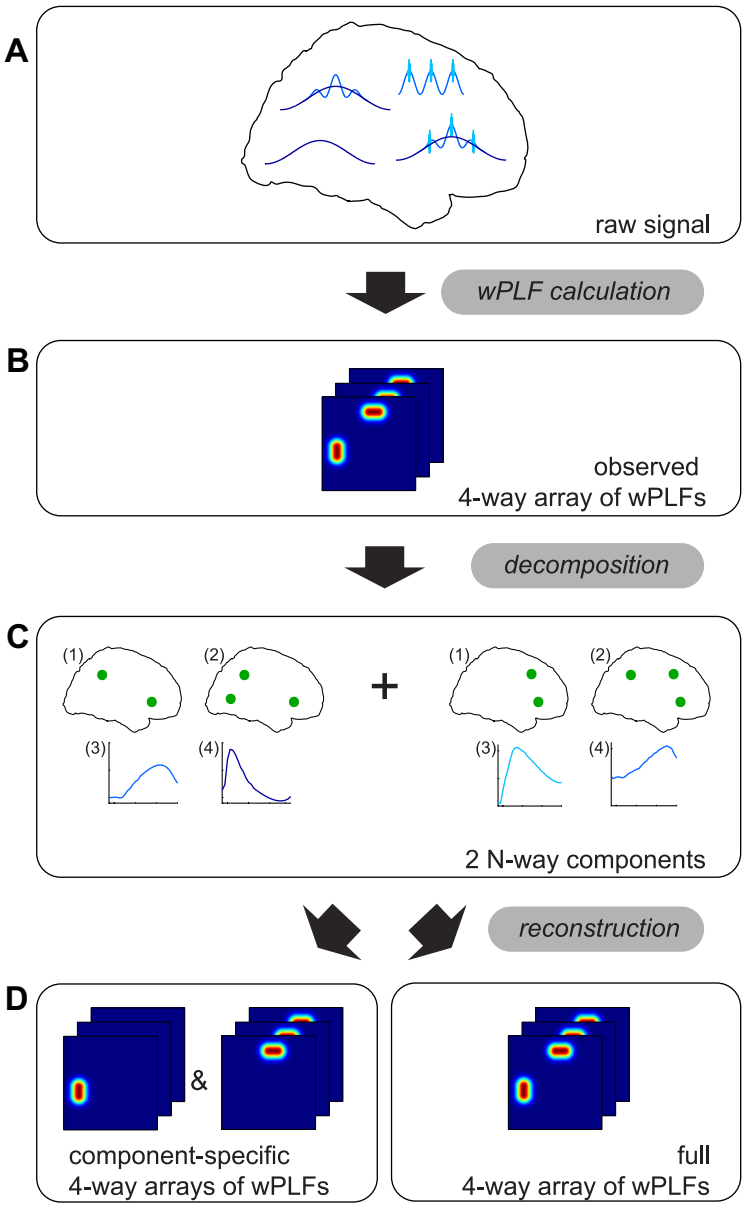

Figure 1. Schematic representation of analyses. The data flow in our analyses is illustrated by a schematic decomposition and reconstruction of two different PAC patterns, one between a slow and a medium fast rhythm, and one between the medium fast and a very fast rhythm. These two PAC patterns have a different spatial distribution. After calculating a 4-way array of wPLFs, the two PAC patterns are separated in two different components using our *N*-way decomposition. The two patterns can then be reconstructed individually into two 4-way arrays of wPLFs or jointly into one 4-way array of wPLFs. For the purpose of simplicity, we have left out phase information in this schematic. Phase information is crucial throughout our analyses and is important for separating PAC patterns. ***A***, PAC at four electrodes involving three oscillations. Not all oscillations are present at each location. ***B***, 4-way array of wPLFs obtained from the raw data in ***A***. The dimensions of this 4-way array are (1) amplitude-providing electrodes, (2) phase-providing electrodes, (3) amplitude-providing frequencies, and (4) phase-providing frequencies. ***C***, Decomposition of the 4-way array of wPLFs in ***B*** into two components. Each component describes one PAC pattern, and each consists of an (1) amplitude-providing spatial map, a (2) phase-providing spatial map, an (3) amplitude-providing frequency profile, and a (4) phase-providing frequency profile. ***D***, Reconstruction of 4-way arrays of wPLFs based on the decomposition in ***C***. On the left, we show the component-specific reconstruction, in which each component is used to create one 4-way array of wPLFs, which is determined by only one PAC pattern. On the right, we show the full reconstruction, resulting in a 4-way array of wPLFs describing both PAC patterns. For details, see Materials and Methods.

and the original array can be reconstructed from its components. There are multiple models for decomposing an *N*-way array, but here we will only describe and use the most parsimonious decomposition, which is based on the PARAFAC model (Harshman, 1970), also known as CANDECOMP (for Canonical Decomposition) (Carrol and Chang, 1970). This decomposition can be derived from a few plausible assumptions about the spatio-spectral characteristics of the sources that are involved in PAC (Maris et al., 2011). Crucially, for *N*-way arrays with more than two dimensions ($N > 2$), *N*-way decomposition based on the PARAFAC model is unique up to scaling and permutation, which are two transformations that do not affect the interpretation of the components. The *N*-way PARAFAC algorithm we used (see below) will be implemented in the FieldTrip open-source MATLAB toolbox (Oostenveld et al., 2011) developed at the Donders Institute for Brain, Cognition and Behavior (http://www.ru.nl/neuroimaging/fieldtrip).

N-way decomposition of 4-way arrays of wPLFs into two complex-valued spatial maps and two frequency profiles. We used *N*-way decomposition based on the PARAFAC model to decompose each 4-way array of wPLFs into one or more components. We show this schematically in Figure 1*C*. Each component consists of four loading vectors, one for each dimension. Because the first two dimensions of a 4-way array of wPLFs correspond to amplitude- and phase-providing electrodes, the corresponding loading vectors in a component describe spatial locations. We denote these two loading vectors as amplitude-providing and phase-providing spatial maps. Furthermore, because the last two dimensions of a 4-way array of wPLFs correspond to amplitude- and phase-providing frequencies, we denote these as amplitude- and phase-providing frequency profiles. Each component thus describes a PAC pattern that is characterized by an amplitude- and phase-providing spatial map and an amplitude- and phase-providing frequency profile.

The decomposition of a single wPLF can be expressed in a formula involving element-wise multiplication:

$$\mathrm{wPLF}_{jklm} = \sum_{f=1}^{F} a_{jf}\, b_{kf}\, c_{lf}\, d_{mf}. \qquad (3)$$

A wPLF_{jklm} is described as the sum, over components *f*, of the product of the loadings a_{jf}, b_{kf}, c_{lf}, and d_{mf}. These loadings are organized in the loading matrices *A*, *B*, *C*, and *D*, respectively. Matrices *A* and *B* contain as columns the amplitude- and phase-providing spatial maps, and matrices *C* and *D* contain as columns the amplitude-and phase-providing frequency profiles. The spatial maps *A* and *B* are complex valued, whereas frequency profiles *C* and *D* are real valued. This differs from the previous approach (Maris et al., 2011), in which only the amplitude-providing spatial map (*A*) was complex valued, reflecting the assumption that there are no between-electrode phase differences in the phase-providing oscillation over electrodes (except for phase differences of exactly $\pm\pi$, which are translated into loadings that have different signs). For our current approach, investigating phase diversity in PAC, it is essential that the phase-providing spatial map *B* is complex valued as well.

Decomposition of preferred coupling phases in PAC into relative phases in two spatial maps. Our *N*-way decomposition decomposes all

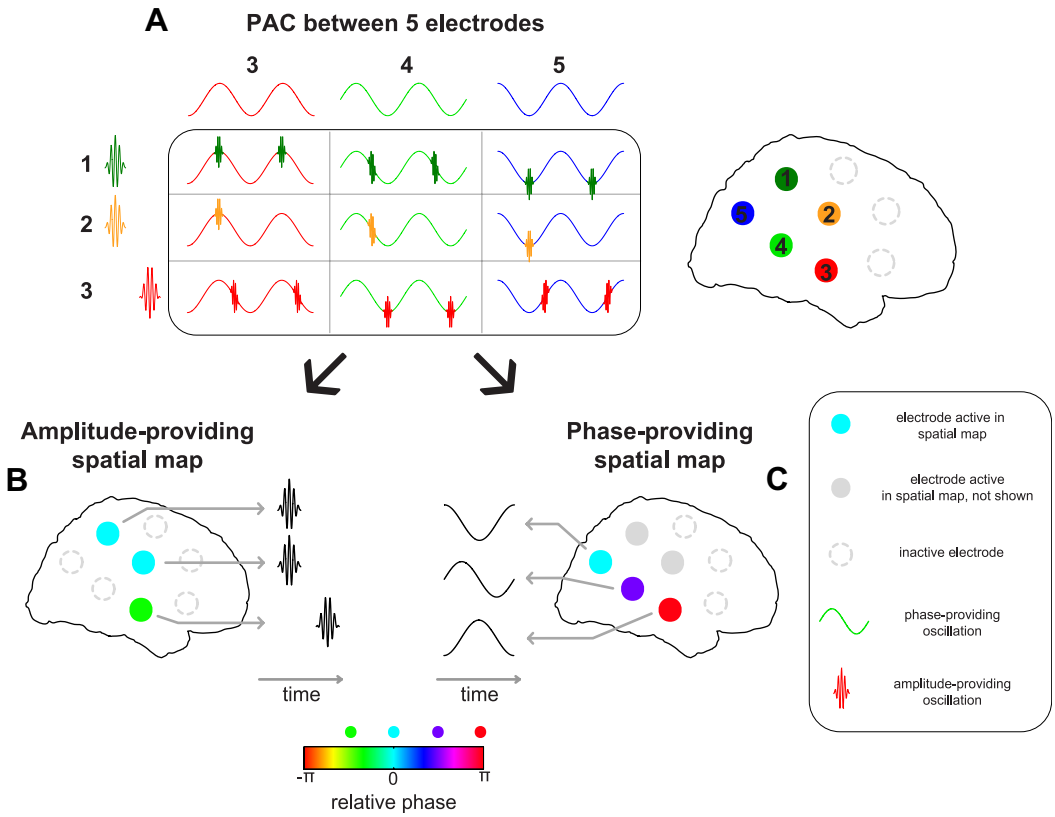

Figure 2. Preferred coupling phases in spatially distributed PAC are decomposed into relative phases in amplitude- and phase-providing spatial maps. Phase diversity of PAC is fully explained by the two complex-valued spatial maps (i.e., phase variability over space). ***A***, Schematic representation of PAC between five electrodes. ***B***, Schematic amplitude-providing spatial map with three electrodes that show amplitude bursts. Color indicates the relative phase of the electrodes. The third electrode has a phase shift of $\pi/2$ relative to the other electrodes. This reflects a time offset of the corresponding amplitude-providing oscillation, given by the phase offset and the cycle length of the phase-providing oscillation in ***C***. ***C***, Same as ***B*** but for the phase-providing spatial map. The phase-providing oscillations have a phase offset equal to their relative phases. Note that we cannot distinguish between the case in which every cycle of the phase-providing oscillation has a burst of the amplitude-providing oscillation (first row of table) and the case in which only some cycles of the phase-providing oscillation have a burst (second row of table).

preferred coupling phases in spatially distributed PAC into two complex-valued spatial maps. As such, phase diversity in PAC is fully explained by the phase relations within the two spatial maps. Phase diversity in the phase-providing spatial map reflects consistent phase differences of the phase-providing oscillation over electrodes. Phase diversity in the amplitude-providing spatial map reflects time delays between amplitude increases of the amplitude-providing oscillation. The exact time delay depends on the cycle length of the phase-providing oscillation. In Figure 2, we show a schematic of this decomposition. This schematic shows PAC between five electrodes (Fig. 2*A*) and their decomposition into an amplitude-providing (Fig. 2*B*) and a phase-providing (Fig. 2*C*) spatial map. The phase relations within the amplitude-providing spatial map reflect between-electrode time delays between bursts of the amplitude-providing oscillations (Fig. 2*B*). The phase relations within the phase-providing spatial map reflect the between-electrode phase differences in the phase-providing oscillations (Fig. 2*C*). Note, we cannot distinguish between (1) the case in which every cycle of the phase-providing oscillation shows a burst of the amplitude-providing oscillation (Fig. 2*A*, first row of table) and (2) the case in which only some cycles show such a burst (Fig. 2*A*, second row of table).

Indeterminacies of the PARAFAC model. The spatial maps and frequency profiles can only be determined up to scaling and permutation. Because of permutation indeterminacy, the order of components is irrelevant, and because of scaling indeterminacy, any loading vector of the same component can be multiplied with any number, as long as another loading vector of the same component is multiplied with the inverse of this number. Moreover, because the two spatial maps are complex valued, there is phase indeterminacy. If one spatial map is multiplied with $e^{-i\theta}$ and the other is multiplied with $e^{i\theta}$, then all phases are shifted by θ, yet the decomposition remains exactly the same. Note that this does not affect the phase differences within a component. Because of the above, the components in our decomposition are sorted by explained variance, all loading vectors are normalized to have a norm of 1, and all spatial maps have an average magnitude-weighted phase of 0. This means that absolute phases inside a spatial map cannot be interpreted. To stress that, within a component, only between-electrode phase differences can be interpreted, the phase of the spatial maps will be denoted as relative phases. Analogously, the magnitude of each electrode in a spatial map and the value of each frequency in the frequency profiles can only be interpreted relative to the other electrodes in the map and the other frequencies in the profile, respectively.

Reconstructing 4-way arrays of wPLFs and evaluating their accuracy. Using the extracted components, we can reconstruct each 4-way array of wPLFs. We computed reconstructions based on all components to evaluate the accuracy of the *N*-way decomposition for every dataset. We also computed reconstructions based on a single component to select significant electrodes in a spatial map. We show both reconstructions schematically in Figure 1*D*. The reconstruction of wPLF x_{jklm} is denoted by $\hat{x}_{jklm}$ and, when based on all components, it is calculated as follows:

$$\hat{x}_{jklm} = \sum_{f=1}^{F} a_{jf}\, b_{kf}\, c_{lf}\, d_{mf}. \qquad (4)$$

Thus, the wPLF at amplitude- and phase-providing electrodes j and k and at amplitude- and phase-providing frequencies l and m can be reconstructed by taking the product $a_{jf}b_{kf}c_{lf}d_{mf}$ and summing over the components. When based on a single component f, $\hat{x}_{jklm}$ is equal to the product $a_{jf}b_{kf}c_{lf}d_{mf}$.

We evaluated the accuracy of reconstructed wPLFs (based on all components) by a coefficient comparing the reconstructed wPLFs to the observed wPLFs. This coefficient was calculated as follows:

$$\text{reconstruction accuracy} = \left| \frac{\langle \overline{\text{vec}(X)}, \text{vec}(\hat{X}) \rangle}{\|X\| \cdot \|\hat{X}\|} \right| \quad (5)$$

We took the inner product $\langle , \rangle$ of the complex conjugate of the vectorized 4-way array of observed wPLFs $\overline{vec(X)}$ and the vectorized 4-way array of reconstructed wPLFs $\text{vec}(\hat{X})$. This inner product is then normalized by the product of the vector norms, and the absolute value is taken. This number ranges from 0 to 1. It can be interpreted as a generalized cosine of the angle between two complex-valued vectors.

Reporting on the results of the N*-way decomposition.* To report the decomposition results, we selected electrodes on the basis of component-specific reconstructed wPLFs. This selection is necessary because we are interested in the phases of the two types of spatial maps, and these phases can only be reliably estimated for electrodes that are involved in the component. We performed our electrode selection by first reconstructing a 4-way array of wPLFs on the basis of a single component (see Materials and Methods). Next, this array of reconstructed wPLFs was compared with the reference distribution from the same dataset (see above, Selecting significant wPLFs). When more than one component was extracted from an array of wPLFs, the same reference distribution was used multiple times. An electrode in the amplitude-providing spatial map was selected if any of the reconstructed wPLFs that have this electrode as the amplitude-providing electrode exceeded the 99th percentile of the reference distribution. The same criterion was applied to the phase-providing spatial maps.

We report on phase differences within each spatial map by computing the difference between pairs of selected electrodes. Among others, we show phase differences occurring between 0 and $\pm\pi$. To demonstrate that these phase differences are reliable (i.e., reflecting true phase differences between 0 and $\pm\pi$), we calculated the split-half reliability of our decomposition results. This involved randomly splitting the trials of each dataset and calculating two 4-way arrays of wPLFs, one for each of the two sets of trials. We then decomposed both arrays into the same number of components and computed the phase differences between pairs of selected electrodes (see above). In addition to this selection based on statistical significance, we selected electrode pairs with phase differences in the intervals from $-2\pi/3$ to $-\pi/3$ and from $\pi/3$ to $2\pi/3$. For these electrode pairs, we calculated the following split-half reliability coefficient:

$$\text{split-half reliability} = \left| \frac{1}{J} \sum_{j=1}^{J} e^{i(\theta_{1j} - \theta_{2j})} \right|. \quad (6)$$

In this formula, we first take the difference between the two independent estimates of the phase difference for electrode pair j, one obtained from the first (θ_{1j}) and the other from the second (θ_{2j}) partition. We do this for all J selected electrode pairs. All phase differences are then expressed as unit-magnitude complex numbers and averaged, producing a mean resultant vector. The split-half reliability coefficient is then obtained by taking the magnitude of this mean resultant vector.

An alternating least-squares algorithm for N*-way decomposition of a 4-way array of wPLFs.* N-way decomposition according to the PARAFAC model can be performed using an alternating least-squares (ALS) algorithm that has been implemented for real-valued arrays (Bro, 1998) and for complex-valued arrays (Sidiropoulos et al., 2000). The algorithm for complex-valued arrays produces only complex-valued components. In contrast, in our application, we decompose a complex-valued array into components that consist of two complex-valued spatial maps and two real-valued frequency profiles. We now describe the algorithm and how we adapted it for complex-valued arrays for our application.

The ALS algorithm is an iterative algorithm with, per iteration, as many steps as the number of different loading matrices. In our case, in every stage of an iteration, a loading matrix least-squares estimate is calculated while keeping the other loading matrices constant. The algorithm continues until an iteration does not provide an increase in fit over and above the previous iteration. All loading matrices are initialized by random starting values, which are orthogonal over components. The algorithm can converge to a suboptimal solution, which is a local minimum of the least-squares objective function that we want to minimize. This is undesirable but can be controlled for by running the algorithm many times with random starting values. If the algorithm converges multiple times to the same solution using different random starting values and this solution also achieves the smallest objective function value, then it is assumed to have converged to the global minimum. It is crucial to detect and discard degenerate models that occur when component pairs are nearly identical but negatively correlated (Bro, 1998). To perform an N-way decomposition based on the PARAFAC model, it is also necessary to estimate the number of components, or the so-called rank of the array. We determined this rank using a split-half procedure, identical to the procedure by Maris et al. (2011).

To describe our ALS algorithm, it is convenient to make use of the Khatri–Rao product $|\otimes|$, which is defined as follows:

$$A| \otimes |B = [a_1 \otimes b_1 \; a_2 \otimes b_2 \ldots a_F \otimes b_F].$$

This applies to any matrix A and B with an equal number of columns F. The Khatri–Rao product is defined as the concatenation of the Kronecker tensor products $\otimes$ of column 1 to F of A and B. Using the Khatri–Rao product, we can express the 4-way PARAFAC model as follows:

$$X^{J \cdot KLM} = A(D| \otimes |C| \otimes |B)^T + E^{J \cdot KLM})$$

In this formula, $X^{J \cdot KLM}$ denotes a 2-way array that is obtained by unfolding the 4-way array X along its last three dimensions. The formula expresses that $X^{J \cdot KLM}$ is the sum of a model term $A(D| \otimes |C| \otimes |B)^T$ and an error term $E^{J \cdot KLM}$. The model term is a function of the loading matrices A, B, C, and D with dimensions $J \times F$, $K \times F$, $L \times F$, and $M \times F$, respectively. F, the number of columns in each loading matrix, denotes the number of components being extracted. In our application, $J = K$ (the number of electrodes), and $L = M$ (the number of frequencies). The error term $E^{J \cdot KLM}$ is necessary to express the fact that the observed wPLFs may differ from the model wPLFs (which are determined by the loadings) as a result of sampling error.

Each least-squares estimate is calculated using the following equation. Because of the symmetry between the four loading matrices, we only present the estimation equations for one loading matrix, which we denote by A. A single iteration of the algorithm estimates all loading matrices once and then determines the fit. By keeping the loading matrices B, C, and D fixed, the least-squares estimation for loading matrix A is the following:

$$A = X^{J \cdot KLM} \cdot \overline{Z} \cdot \overline{(Z^{\star} Z)^{+}}, \quad (7)$$

where $Z = (D|\otimes|C|\otimes|B)$, $\bar{Z}$ denotes the complex conjugate of Z, $Z^{\star}$ denotes the complex conjugate transpose of Z, and $+$ denotes the Moore–Penrose pseudoinverse. The least-squares estimate of a real-valued loading matrix (matrices C and D) is obtained by replacing Z and X by the real-valued matrices $Z = [Re(Z) \; Im(Z)]$, which is the row-wise concatenation of $Re(Z)$ and $Im(Z)$ (the real and the imaginary parts of Z) and $X = [Re(X) \; Im(X)]$, which is the column-wise concatenation of $Re(X)$ and $Im(X)$.

Results

We analyzed PAC in human ECoG recordings from 42 datasets obtained from 27 patients performing a working memory task (see Materials and Methods). We investigated the phase diversity of spatially distributed PAC by means of wPLFs. These wPLFs are complex-valued association measures, quantifying coupling between the phase of one oscillation and the amplitude of another, averaged over time (see Materials and Methods). Our wPLF is a correlational and not a causal measure. To reflect this, we use the causally neutral terms "phase-providing" and "amplitude-providing" to denote the first and the second oscillation, respectively. wPLFs were computed for all amplitude- and phase-providing electrodes and frequencies. This results in a 4-way

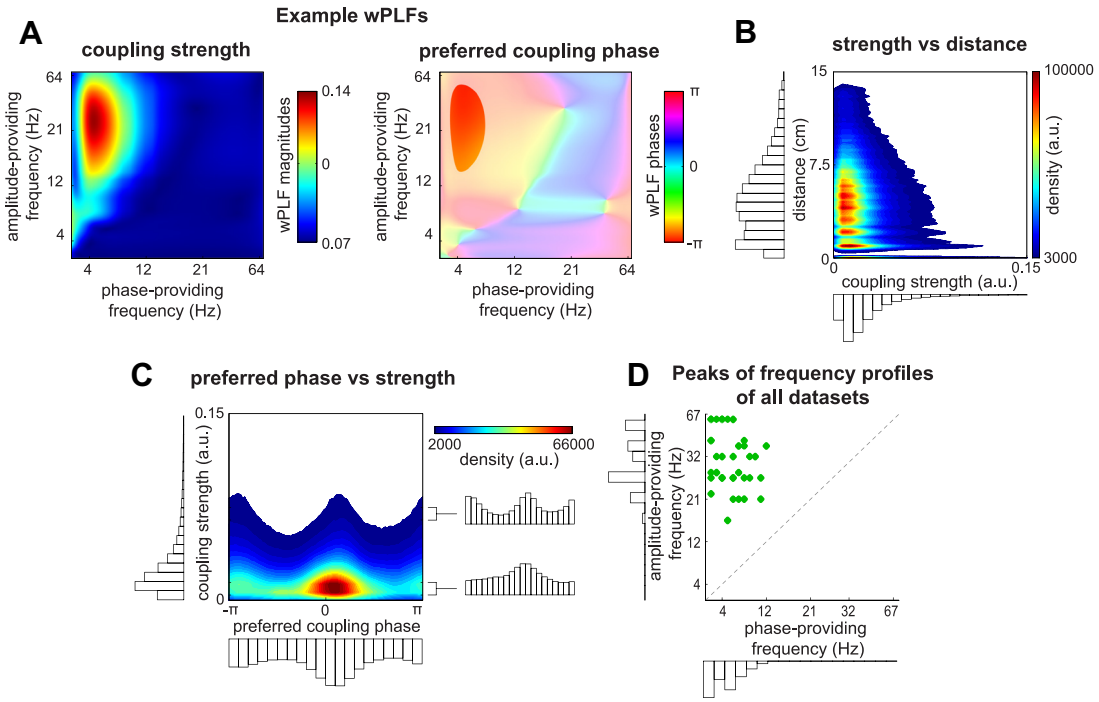

Figure 3. PAC occurred over long distances, has diverse preferred coupling phases, and involved many frequencies. ***A***, Example wPLFs for one electrode pair. For this electrode pair, the strongest coupling is between the phase of a theta oscillation (~3–8 Hz) and the amplitude of a beta/gamma oscillation (~18–42 Hz). The preferred coupling phase is π, which corresponds to the trough of the theta oscillation. Color bar codes reflect wPLF magnitude and phase. ***B***, Density of the significant wPLFs from all datasets as a function of their strength and the distance between the amplitude- and phase-providing electrodes. The majority of PAC occurs at distances ~6 cm and can go up to ~14 cm. Color bar code reflects the density of wPLFs at each *X*–*Y* coordinate. ***C***, Density of the significant wPLFs as a function of their preferred coupling phase and their strength. PAC occurs with diverse preferred coupling phase, with most preferred phases around the peak of the phase-providing oscillation (angle = 0). However, especially for the wPLFs that show a strong coupling, preferred phases also cluster at the trough (angle = $\pm\pi$). Color bar code same as in ***B***. ***D***, Scatter plot of the peaks of the frequency profiles obtained from the significant wPLFs (see Materials and Methods). The peak phase-providing frequencies show a substantial spread, ranging from delta to alpha, and so do the amplitude-providing frequencies, ranging from beta to gamma.

array of wPLFs. As an example, we show one slice of such a 4-way array (Fig. 3*A*), containing the wPLFs for all frequency pairs and a single electrode pair. For this electrode pair, the strongest coupling is between the phase of a theta oscillation (center frequency, 6 Hz) and the amplitude of a beta/low-gamma oscillation (center frequency, 23 Hz). The preferred coupling phase is π, which corresponds to the trough of the theta oscillation.

We used two approaches to investigate phase diversity in spatially distributed PAC, one based on selecting significant wPLFs from the 4-way arrays (one array for every dataset) and the other based on a decomposition of each of these arrays. We first report on the results obtained by selecting significant wPLFs, showing that PAC occurred over long distances with substantial phase diversity. Next, we report on the decomposition results, showing that this phase diversity originated mainly from the spatially distributed phase-providing oscillations.

PAC occurred over long distances, involved diverse preferred coupling phases, and involved many frequencies

We selected statistically significant wPLFs from each of the 42 datasets. Significance was assessed by comparing every wPLF with a reference distribution obtained under the null hypothesis of independence of phases and amplitudes (see Materials and Methods). wPLFs were selected if their magnitude exceeded the 99th percentile of this distribution. On average, 15.7 ± 9.0% (SD) of the wPLFs were selected from each of the 42 datasets. These were combined into one large data array used for all analyses on significant wPLFs. The contribution of each of the 42 datasets to this data array was on average 2.4 ± 2.3% (SD), and the contribution of each of the 27 patients was on average 3.7 ± 3.5% (SD).

To investigate the spatial extent of the observed PAC, we computed the Euclidian distance (using Talairach coordinates) between all electrode pairs involved in the significant wPLFs. We constructed the density of wPLFs as a function of their strength (horizontal axis) and the distance between electrodes within a pair (vertical axis) (Fig. 3*B*). We observed that (1) PAC occurred predominantly at distances ~6 cm, (2) PAC occurred at distances as large as 14 cm, and (3) PAC strength decreased with distance.

Next, we investigated the diversity in preferred coupling phases. We constructed the density of significant wPLFs as a function of their phase and their strength (Fig. 3*C*). We make the following three observations: (1) PAC occurred with diverse preferred coupling phases, (2) for weak coupling, phases were clustered around the peak of the phase-providing oscillation (phase = 0), and (3) for strong coupling, phases were clustered both around the peak and the trough (phase = $\pm\pi$). The observed diversity in preferred coupling phase is not produced by sampling error resulting from unreliable phase estimates (Fig. 4).

We obtained peaks of frequency profiles of the amplitude- and phase-providing frequencies of the significant wPLFs for each dataset by counting the significant wPLFs in the three other dimensions. We constructed a scatter plot (Fig. 3*D*) and observed that PAC involved many frequencies. The peak phase-providing frequencies showed a substantial spread, ranging from delta (2 Hz or lower) to alpha (12 Hz), and so do the amplitude-providing frequencies, ranging from alpha (15 Hz) to gamma (67 Hz or higher).

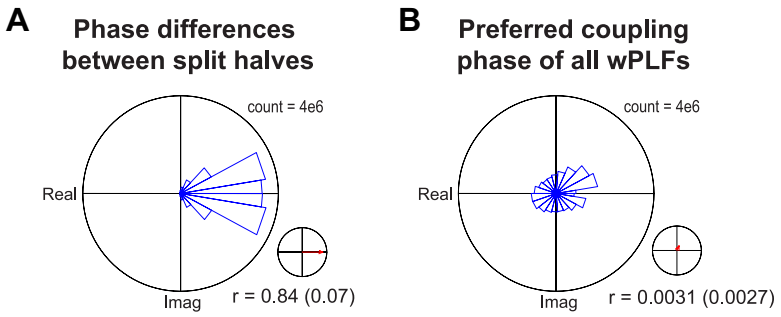

Figure 4. Diversity in preferred coupling phase is produced by reliable phase estimates. To estimate the reliability of our phase estimates, we randomly partitioned the trials of each dataset into two sets. A 4-way array of wPLFs was then calculated for each of the two sets of trials. ***A***, Histogram of phase differences between wPLFs of the first and the second set of trials for all datasets. The majority of phase differences are very close to 0, indicating that the preferred coupling phases are highly similar in the two sets of trials. The reliability coefficient, calculated on these phase differences (see Materials and Methods), was on average 0.84 ± 0.07 (SD). ***B***, For comparison with the reliability results in ***A***, we show the same information for the preferred coupling phase of the wPLFs, instead of their between-set phase differences. The phase histogram shows diversity in preferred coupling phase (same information as in Fig. 3*C*). We calculated the same coefficient as in ***A*** but now applied to the preferred coupling phase (instead of the between-set phase differences) and found that it was on average 0.0031 ± 0.0027 (SD). The difference with the average reliability coefficient shows that our phase estimates are highly reliable.

From our analysis of significant wPLFs, we conclude that PAC (1) occurred over long distances, (2) showed substantial diversity in preferred coupling phases, and (3) involved many frequencies. However, analyzing significant wPLFs does not inform us about the spatial distribution of PAC or the origin of the phase diversity. More specifically, we do not know (1) whether the observed long-distance PAC is generated by multiple small spatially separated sources or by one very large source, (2) whether the phase diversity is attributable to phase differences within a source or between sources, or (3) how the spatial distribution of the phase-providing electrodes is related to that of the amplitude-providing electrodes. To investigate these issues, we decomposed each 4-way array of wPLFs into sets of two spatial maps and two frequency profiles. Importantly, these spatial maps provide information about the spatial distribution of PAC and the origin of the phase diversity.

N-way decomposition reveals the spatial distribution of PAC in sets of two spatial maps and two frequency profiles

To analyze the spatial distribution and phase diversity of PAC, we used *N*-way decomposition based on the PARAFAC model (see Materials and Methods). This method has been used previously (Maris et al., 2011) but in a version that was unable to reveal the phase diversity that we identified (see Materials and Methods). Each 4-way array of wPLFs was decomposed into one or more components. Every component characterizes one PAC pattern and consists of an amplitude-providing and a phase-providing spatial map and an amplitude-providing and a phase-providing frequency profile. Because a dataset may involve multiple PAC patterns, the decomposition can extract multiple components. To illustrate the decomposition, we show an example component of a representative subject (Fig. 5). The spatial maps are shown as grids on a template brain (Fig. 5*A*,*B*; not all ECoG grids are shown), and the frequency content is shown in the frequency profiles (Fig. 5*C*). With respect to the example component, we observed that (1) both the amplitude-providing (Fig. 5*A*) and the phase-providing (Fig. 5*B*) spatial map had a wide spatial distribution over cortex, (2) the phase-providing spatial map had a wider spatial distribution than the amplitude-providing spatial map, and (3) there was more phase diversity in the phase-providing than in the amplitude-providing map (Fig. 5*A*). These observations are representative for all 42 datasets. Note that the phase-providing spatial map in the example component shows a spatial structure similar to that of traveling waves. This was the case for 42 of 85 components.

The example component (Fig. 5*A–C*) reflects the main pattern in the original 4-way array of wPLFs. To show this, we selected two electrode pairs that share the same amplitude-providing electrode (electrode 43) but have different phase-providing electrodes (electrodes 29 and 57). We show the wPLFs for both pairs, for all frequency pairs (Fig. 5*D*). The frequencies that exhibit strong coupling closely match the frequency profiles from the decomposition (Fig. 5*C*). Moreover, the phase difference between the two electrode pairs closely match the phase differences in the phase-providing spatial map (Fig. 5*B*). [Note that, in contrast to between-electrode phase differences, absolute phases cannot be interpreted (see Materials and Methods).] It is important to note that relative phases in amplitude- and phase-providing spatial maps reflect different properties of spatially distributed PAC (Fig. 2; see Materials and Methods). From the 42 datasets, we extracted 85 components, explaining on average 50.7 ± 20.1% (SD) of the variance of significant wPLFs. We evaluated the accuracy of the reconstruction of all preferred coupling phases. For the phases of all significant wPLFs, we compared their reconstructed and their corresponding observed values. All magnitudes were set to 1. For every dataset, we calculated a coefficient that quantified reconstruction accuracy (see Materials and Methods), which ranges from 0 to 1. This coefficient of reconstruction was on average 0.70 ± 0.15 (SD), indicating that the observed wPLFs can be accurately reconstructed from the decompositions.

We now show two sets of aggregated results obtained from all components. First, we investigated the spatial extent of the spatial maps. We constructed a scatter plot of the mean between-electrode Euclidian distance of each spatial map per component (Fig. 6*A*). We selected electrodes in each spatial map by comparing the component-specific reconstructed wPLFs to the 99th percentile of the reference distribution used to select significant wPLFs (see Materials and Methods). The mean distance was on average higher for the phase-providing than for the amplitude-providing spatial maps (paired samples *t* test; $t_{(84)} = -5.56, p < 1e\text{-}6$). This shows that our PAC was not generated by distributed sharp-edged waveforms because both maps would be equally large. This issue has been discussed previously (Maris et al., 2011).

Second, we investigated the frequency profiles of the amplitude- and phase-providing oscillations of all components. We constructed a scatter plot of the peaks of the amplitude- and phase-providing frequency profiles (Fig. 6*B*). Peaks of the phase-providing frequency profiles were spread out, ranging from delta (~2 Hz) to alpha (~16 Hz). Peaks of amplitude-providing frequency profiles were spread out even more, ranging from theta (~5 Hz) to gamma (~67 Hz or higher). Note the difference with Figure 3*D*. The peak frequencies determined from the decomposition (Fig. 6*B*) showed a much larger spread than to those from the 4-way array of wPLFs (Fig. 3*D*). This most likely results from the fact that each 4-way array of wPLFs carries several PAC patterns.

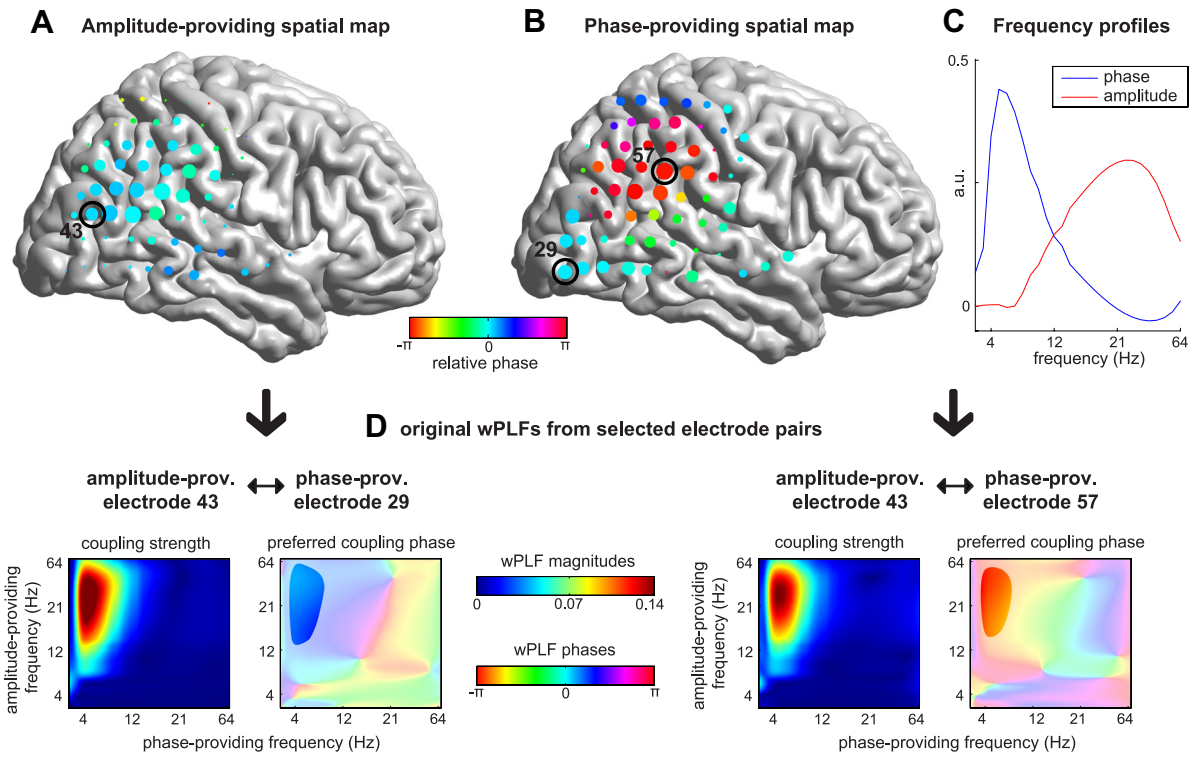

Figure 5. *N*-way decomposition reveals the spatial distribution in PAC in sets of two spatial maps and two frequency profiles. Each 4-way array of wPLFs from each dataset was decomposed into one or more components, each component being a set of two spatial maps and two frequency profiles. The diversity in the preferred coupling phase is explained by the two complex-valued spatial maps, namely by their phase diversity across space. ***A–C***, Example component from a representative subject. ***A***, Amplitude-providing spatial map. ***B***, Phase-providing spatial map. Both the amplitude- and phase-providing spatial map are widely distributed over the cortex, but the phase-providing spatial map is wider and shows more phase diversity. The size of the markers indicates the contribution of each electrode to the spatial map, and the color indicates the relative phase of the electrodes. ***C***, Amplitude- and phase-providing frequency profiles. These profiles show that the example component involves a coupling between the phase of a theta oscillation and the amplitude of a beta/gamma oscillation. ***D***, wPLFs (for all frequency pairs) of two selected electrode pairs. The frequency pairs for which there is strong coupling closely match the frequency profiles in ***C***, and the difference between the preferred coupling phases closely match the corresponding phase difference in the phase-providing spatial map.

Phase-providing and amplitude-providing spatial maps show different phase configurations

To investigate the phase configuration within both types of spatial maps, we calculated the phase differences for all possible pairs of electrodes selected from a spatial map (Fig. 7). As before, we selected electrodes based on the component-specific reconstructed wPLFs (see Materials and Methods). To show the aggregate phase diversity in both spatial maps, we show the density of electrode pairs as a function of their strength and their phase difference (Fig. 7*A*,*B*). We observe (1) that both amplitude- and phase-providing spatial maps showed phase differences clustered around 0, (2) that phase-providing spatial maps also showed phase differences clustered around $\pm\pi$, and (3) that both maps showed phase differences between 0 and $\pm\pi$. This indicates that the amplitude-providing spatial maps mainly showed synchronous phase configurations. Conversely, the phase-providing spatial maps also showed so-called anti-phasic configurations, with two groups of electrodes having small within-group but large between-group phase differences. Importantly, both maps showed phase differences between 0 and $\pm\pi$. Modulation of phase relations across the complete circle (not limited to synchrony/anti-phase) may

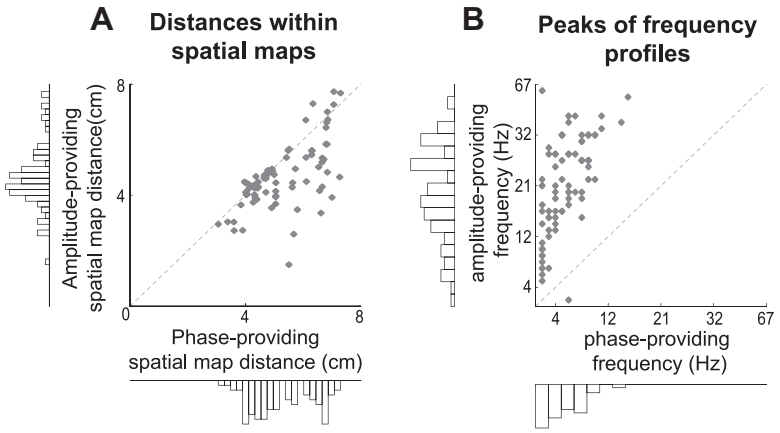

Figure 6. Spatial extent of spatial maps and frequency profiles. ***A***, Mean distance within components in phase-providing spatial maps (horizontal axis) plotted against the mean distance in amplitude-providing spatial maps (vertical axis). The mean distance within components was on average higher for the phase-providing than for the amplitude-providing spatial maps (paired samples *t* test; $t_{(84)} = -5.56, p < 1e\text{-}6$). ***B***, Scatter plot of the peaks of the phase-providing frequencies (horizontal axis) versus the peaks of the amplitude-providing frequencies (vertical axis). There is a substantial spread of the peaks of the phase-providing frequency profiles, ranging from delta to alpha, and those of the amplitude-providing frequency profiles, ranging from theta to gamma. Note the difference with respect to Figure 3*D*, and see Results for a possible explanation. For selection of electrodes, see Materials and Methods.

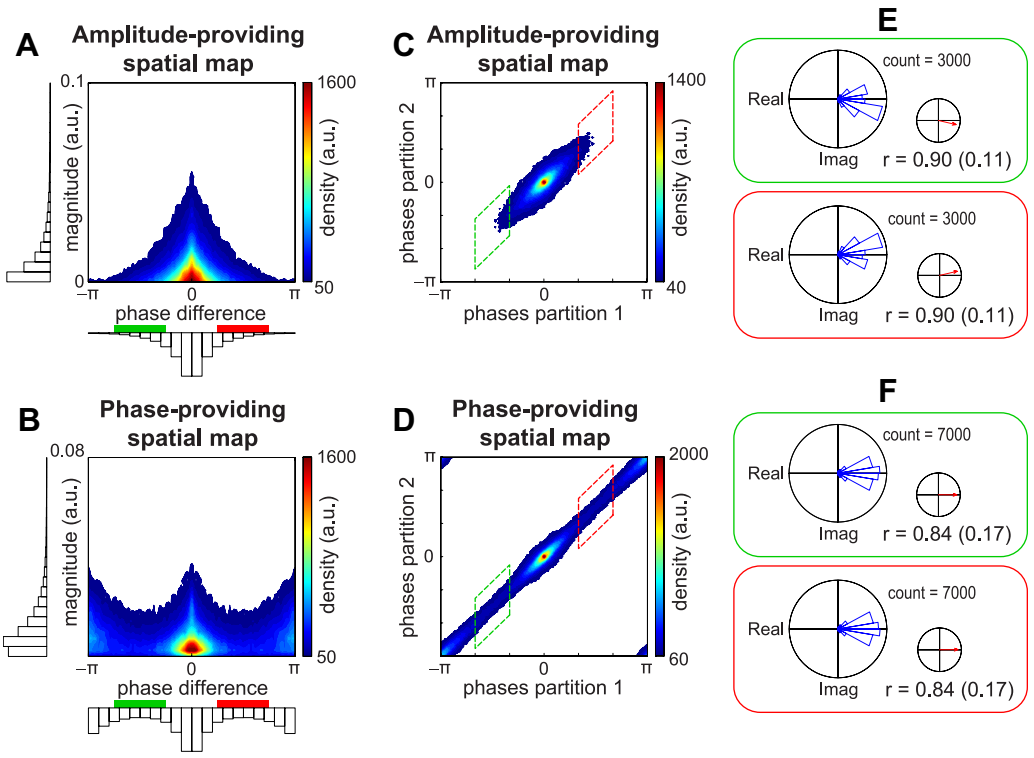

Figure 7. Phase-providing and amplitude-providing spatial maps show different phase configurations. To investigate the phase configurations of both types of spatial maps, we computed the phase differences for all possible pairs of electrodes selected from a spatial map. ***A***, Density of electrode pairs of each spatial map as a function of their magnitude and their phase differences for the amplitude-providing spatial map. Phase differences cluster around 0. ***B***, Same as in ***A*** but for the phase-providing spatial map. Phase differences are mostly around 0 and $\pm\pi$. ***C–F***, To investigate the reliability of the phase differences, we evaluated the split-half reliability of our decomposition results (see Results and Materials and Methods). ***C***, Density of amplitude-providing spatial map phase differences from the first versus those of the second set. ***D***, Same information as in ***C*** but for phase-providing spatial maps. Between-set phase differences are highly similar for both spatial maps, showing that they are highly reliable. ***E***, Phase histograms and mean resultant vector of the amplitude-providing spatial map between-set phase differences for the intervals from $-2\pi/3$ to $-\pi/3$ (green box) and from $\pi/3$ to $2\pi/3$ (red box). ***F***, Same as in ***E*** but for the phase-providing spatial maps. For both types of spatial maps, between-set phase differences cluster around 0, indicating reliability of the between-electrode phase differences in this narrow range. For a description of the reliability coefficient r, see Results. For selection of electrodes, see Materials and Methods.

have important consequences for the computational mechanism that PAC reflects. More specifically, if PAC reflects selective routing of information by modulating excitability of neuronal groups, then phase determines its flexibility.

From this perspective, it is crucial to establish that the observed phase differences between 0 and $\pm\pi$ are not estimation errors but true phase differences. To demonstrate this, we evaluated the split-half reliability of these phase differences. For each dataset, we randomly partitioned trials in two sets and calculated 4-way arrays of wPLFs for both. We then decomposed each array into the same number of components and computed phase differences as above. We show the split-half reliability as the density of between-electrode phase differences from the first set of trials plotted against those of the second set (Fig. 7*C*,*D*). We observe that all phase differences were highly similar between the two sets of trials, and this holds for both spatial maps. Thus, phase differences in the decomposition reflect true phase differences. As an additional quantification, we calculated differences between the two sets of phase differences (Fig. 7*E*,*F*). We selected phase differences between $-2\pi/3$ to $-\pi/3$ and $\pi/3$ to $2\pi/3$, as estimated using the first set of trials. For both types of spatial maps, between-set phase differences cluster around 0 (Fig. 7*E*,*F*). This indicates that, even for this narrow range, the phase differences reflect true phase differences. To support this quantitatively, we computed a reliability coefficient, ranging from 0 to 1 (see Materials and Methods). For both spatial maps, the coefficient r was high for both intervals (Fig. 7*E*,*F*).

Different connectivity structure for components with different phase-providing frequencies

To reveal the connectivity structure of PAC in our 85 extracted components, we aggregated over all pairs of selected electrodes (Fig. 8). As before, we selected electrodes based on the component-specific reconstructed wPLFs (see Materials and Methods). To visualize the connectivity structure, we downsampled the anatomical locations of electrodes (using Talairach coordinates) to 23 locations on the left and 23 locations on the right hemisphere. We did not observe all possible connections based on these downsampled locations: of the 2116 possible connections, we observed 1698 (80.3%) in our data. However, as will become clear, our quantifications and subsequent comparisons were not biased by this incompleteness. For every observed connection, we calculated the proportion selected electrode pairs within a downsampled connection. This proportion estimates the probability that PAC is found between the downsampled locations. The number of electrode pairs over which this proportion was calculated differed greatly across location pairs. This was especially the case for the small number of contralateral versus the large number of ipsilateral electrode pairs (Fig. 8*C*).

We use connectograms to show the connectivity structure of PAC (Fig. 8*A*). Whereas no clear structure is revealed by the connectogram for all components together (Fig. 8*A*, top connectogram), much structure is revealed when separate connectograms are made for components with different phase-providing frequencies (Fig. 8*A*, three bottom connectograms). In these

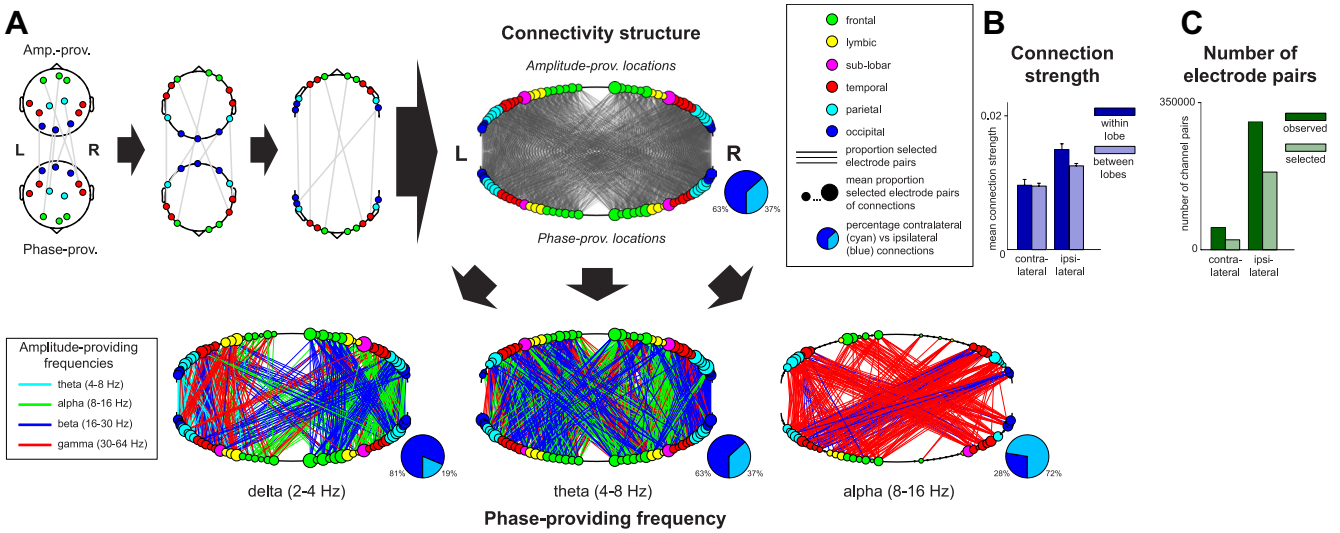

Figure 8. Differential connectivity structure in PAC components with different phase-providing frequencies. To investigate the connectivity structure in PAC, we aggregated over all pairs of selected electrodes from all 85 *N*-way components (for electrode selection, see Materials and Methods). The original Talairach-based locations were downsampled to 23 unique locations on both the left and the right hemisphere. Every resulting connection was indexed by the proportion of its electrode pairs that were selected. Note that not all possible connections were observed in the data (see Results). ***A***, Connectograms. Schematic on the left depicts the construction of a connectogram for a set of connected electrodes. In all connectograms, line thickness indicates the proportion of selected electrode pairs within a downsampled connection (if a proportion is 0, the line is absent). Furthermore, node color indicates lobe, and node size indicates the sum of the proportions of selected electrode pairs of all its connections. Pie charts indicate the number of non-zero ipsilateral versus contralateral connections within a connectogram. The bottom three connectograms were obtained by splitting the connections according to their phase-providing frequency. In these connectograms, line color indicates the amplitude-providing frequency of the connection. Because of spatial downsampling, every connection represents many electrode pairs from multiple *N*-way components. The frequency color code was based on the mode of the distribution (over electrode pairs) of the associated peak frequency profiles. Components that differ in the frequency of their phase-providing oscillation have connectograms that differ greatly in their connectivity pattern, including their degree of cross-hemispheric lateralization. ***B***, Mean of the contralateral versus ipsilateral and the within- versus between-lobe connection strengths. Means are taken over the median connection strength of the electrode pairs forming a connection. The connection strengths were computed by selecting their component-specific reconstructed wPLFs and taking a weighted average over the two frequency dimensions. ***C***, Number of electrode pairs selected and observed for contralateral and ipsilateral connections.

connectograms, line color indicates the amplitude-providing frequency of each connection; pie charts show the percentage of non-zero contralateral and ipsilateral connections. Because of spatial downsampling, every connection consists of many electrode pairs from multiple components. The frequencies used for the connectograms were obtained by taking the mode over the peaks of all their frequency profiles. Components that differ in their phase-providing frequency differ greatly in their connectivity pattern, including their degree of cross-hemispheric lateral connections. We observe that (1) delta oscillations show mostly ipsilateral connections, (2) theta oscillations show both ipsilateral and contralateral connections, and (3) alpha oscillations show predominantly contralateral connections. The imbalance of contralateral versus ipsilateral connections in the top connectogram is partly the result of the relatively small number of patients with bilateral recordings sites (11 of 27). This source of the imbalance also affects the bottom three connectograms, whose combination forms the top connectogram. Importantly, because this source of imbalance affects all bottom three connectograms to the same extent, their number of contralateral connections can be safely compared with each other.

Our findings were obtained by investigating the number of connections that exist between downsampled locations. We also investigated the coupling strength between these locations, calculated as the median connection strength over all electrode pairs belonging to that connection. For each electrode pair, connection strength was calculated by selecting their component-specific reconstructed wPLFs and taking a weighted average over the two frequency dimensions. We now report on this, with separate averaging over (1) contralateral and ipsilateral and (2) within- and between-lobe connections (Fig. 8*B*). We observe that (1) there is only a small difference in connection strength between lobes compared with within lobes, and (2) the contralateral and ipsilateral connection strengths did not differ greatly: the average strength of the contralateral connections was 69.7% of the average strength of the ipsilateral connections (Fig. 8*B*). We also investigated the above patterns separately for each of the three phase-providing frequencies (delta, theta, and alpha), but we found no substantial differences (figure not shown).

Discussion

We provided evidence for three key properties that could allow PAC to flexibly and selectively route information through distributed neuronal networks. (1) We showed that PAC was widely spatially distributed. From our analyses of significant wPLFs, we found that PAC occurred at distances >10 cm. Using a decomposition based on the PARAFAC model, we showed that this PAC was generated by spatially distributed phase- and amplitude-providing oscillations, of which the phase-providing oscillations were more spread out. The spatial distribution of PAC is required to be able to route information through distributed networks. (2) We showed that, over these spatially distributed networks, there was great phase diversity. The phase diversity we observed was mainly explained by phase diversity in the phase-providing oscillation, showing phase differences over space, across the whole circle. This phase diversity can determine the flexibility of PAC in selecting neuronal populations for interaction. (3) We showed that PAC occurred between oscillations of many different frequencies (He et al., 2010; Miller et al., 2010; Maris et al., 2011). Amplitude-providing frequencies ranged from theta to gamma, and phase-providing frequencies ranged from delta to alpha. This

frequency diversity can determine the flexibility of PAC in separating neuronal networks operating in parallel.

Besides providing evidence for these three key properties, we also made a first step toward identifying different roles for phase-providing oscillations at different frequencies. We showed that delta oscillations establish mostly ipsilateral connections, theta oscillations establish both ipsilateral and contralateral connections, and alpha oscillations establish predominantly contralateral connections.

Although we find PAC that is widely spatially distributed, most reports so far have shown local PAC (Chrobak and Buzsáki, 1998; Lakatos et al., 2005; Mormann et al., 2005; Canolty et al., 2006; Cohen, 2008; Lakatos et al., 2008; Osipova et al., 2008; Penny et al., 2008; Axmacher et al., 2010; He et al., 2010; Miller et al., 2010; Voytek et al., 2010). The evidence for cross-area PAC is much less abundant (Sirota et al., 2008; Tort et al., 2008; Maris et al., 2011). This is surprising given that, at least for theta, oscillations are measurable over broad regions (von Stein and Sarnthein, 2000; He et al., 2008).

PAC is a form of oscillatory synchronization that involves two different frequencies. A more familiar form of oscillatory synchronization involves only a single frequency: phase consistency between oscillations. This type of oscillatory synchronization was originally put forward as a mechanism to bind different features of an object, encoded in different neuronal populations, and was confined to gamma (Singer and Gray, 1995; Singer, 1999). More recently, it has been proposed as a mechanism of communication between neuronal groups (Fries, 2005). Central to this proposal is that neurons preferably fire in a specific phase of the gamma cycle, implying a temporal relation between spikes of coherently oscillating neurons. This allows neurons to synchronize their periods of maximum excitability and communicate effectively. An expanded mechanism, involving PAC, would be that the phase-providing oscillation modulates when neuronal populations engage in oscillatory phase synchronization. Such a mechanism would require phase consistency during high-frequency bursts. Although we did not investigate this, long-range phase consistency at high frequencies has been reported (Gregoriou et al., 2009). If it is indeed the case that phase-providing oscillations select neuronal populations for communication, then such cross-frequency interaction could provide dynamic gating of information (Vogels and Abbott, 2009; Akam and Kullmann, 2010). The phase-providing oscillation as a selector would also greatly benefit from a process that creates substantial phase diversity across sites, which we have observed, in which site-specific phases could function as a selection variable. Besides the separation of neuronal activity via phase diversity (i.e., "phase multiplexing"), the separation of multiple networks operating in parallel could also be supported by frequency diversity (i.e., "frequency multiplexing").

Although we provide evidence for three key properties that makes PAC a likely candidate for routing for information, we do not have a mechanistic neurophysiological model to explain our observations, and providing such an explanation is a crucial challenge for future research. Obviously, neuronal spiking is the signal for targeted communication between neurons. Therefore, we face the challenge to link our findings using ECoG to neuronal signals with a very different spatial specificity. Inevitably, any attempt to provide such a link will involve some speculation. However, it is justified to the extent that it can be related to relevant findings in the literature. We hypothesize that PAC may reflect an interaction between slow and fast rhythmic synaptic input streams and that the efficacy of this interaction can be modulated by adjusting the timing between these rhythms. Furthermore, we hypothesize that the slow rhythm, the phase-providing oscillation, can be used to segregate information streams by variations in its phase over space. These hypotheses have links with the substantial literature on up and down states (Steriade et al., 1993; Destexhe et al., 2003; Cash et al., 2009; Haider and McCormick, 2009).

Up and down states are brain states that can be characterized at many levels, ranging from intracellular recordings to macroscopic electroencephalography (Steriade et al., 2001; Destexhe et al., 2003; Volgushev et al., 2006). Up and down states are most easily identified during slow-wave sleep and anesthesia, when they alternate rhythmically (Hô and Destexhe, 2000; Sanchez-Vives and McCormick, 2000; Shu et al., 2003; Hasenstaub et al., 2005; Haider et al., 2006). This typically occurs at a frequency <1 Hz, producing the so-called cortical slow oscillation. During wakefulness and shallow sleep, isolated down states called K-complexes occur in a nonrhythmic manner, sometimes preceded by an up state (Amzica and Steriade, 1997; Cash et al., 2009). In both rhythmic and nonrhythmic cases, up and down states are spatially distributed (Volgushev et al., 2006). Furthermore, recordings in animals (Sanchez-Vives and McCormick, 2000; Volgushev et al., 2006) and humans (Massimini et al., 2004) have shown that the cortical slow oscillation is phase diverse over space. In ECoG recordings, up and down states can be identified as positive and negative deflections (Cash et al., 2009). These originate from a source-sink configuration, with a source in layer II/III and a sink in layer I (Cash et al., 2009). The neocortical up state is a network phenomenon, characterized by a balance in excitatory and inhibitory input (Haider et al., 2006). During an up state, neurons have an increased membrane potential, bringing them closer to their firing threshold (Haider et al., 2007). Animal studies have shown that, during an up state, there is an increase in spiking activity and high-frequency (30–100 Hz) local field potential (LFP) fluctuations (Nowak et al., 1997; Haider and McCormick, 2009). A down state provides the opposite: the membrane potential is hyperpolarized, and there is a strong decrease in spiking and high-frequency LFP fluctuations.

The rhythmic alternation of up and down states has similarities to our PAC results: (1) it involves a slow oscillation with high-frequency oscillations occurring at specific phases, (2) the slow oscillation is spatially distributed, and (3) the slow oscillation is phase diverse over space. Based on these similarities, we propose that phase-providing oscillations of PAC could affect neuronal populations in a similar way. The phase-providing oscillation could, like the cortical slow oscillation, modulate the basal membrane potentials of neuronal groups, which could provide joint windows of communication during certain phases. This could allow neuronal groups to exchange information during bursts of high-frequency LFP fluctuations. This information exchange could involve coherent oscillations. Importantly, there are a number of differences between up and down states, and our PAC results complicate this comparison. First, slow cortical oscillations are typically <1 Hz, whereas we identified phase-providing oscillations between 2 and 16 Hz (lower boundary is restricted by epoch length). Second, the phase diversity we observed across space is much larger than the phase diversity in the slow oscillation. Last, high-frequency LFP fluctuations during up states are locked to the peak of the slow oscillation, whereas we report strong diversity in preferred coupling phases of PAC. The reported phase of the slow oscillation, however, depends on where in the neuropil the signal is recorded: because the up and down states are characterized by a source-sink configuration between layer I and layer II/III (Cash et al., 2009), the polarity of the slow oscillation would reverse if one would record from layer

II/III. Assuming that the neurophysiological makeup of the brain allows for different source-sink configurations across layers, it should be possible to generate PAC with diverse phases as measured on the surface of the brain.

More evidence is needed to show that spatially distributed PAC in ECoG signals reflect a neurophysiological mechanism that also modulates spiking activity. At least part of the evidence must come from *in vivo* experiments involving simultaneous recordings from multiple sites in the neuropil. The present study can guide the analysis of these recordings. We have demonstrated that PAC is a pervasive phenomenon that has a wide spatial distribution, a strong diversity in preferred coupling phases, and involves oscillations at many frequencies. With these properties, PAC is a plausible candidate for supporting selective neuronal communication.

References

Akam T, Kullmann DM (2010) Oscillations and filtering networks support flexible routing of information. Neuron 67:308–320.

Amzica F, Steriade M (1997) The K-complex: its slow (<1-Hz) rhythmicity and relation to delta waves. Neurology 49:952–959.

Axmacher N, Henseler MM, Jensen O, Weinreich I, Elger CE, Fell J (2010) Cross-frequency coupling supports multi-item working memory in the human hippocampus. Proc Natl Acad Sci U S A 107:3228–3233.

Beckmann CF, Smith SM (2005) Tensorial extensions of independent component analysis for multisubject FMRI analysis. Neuroimage 25:294–311.

Bro R (1998) Multi-way analysis in the food industry. Models, algorithms, and applications. Amsterdam: University of Amsterdam.

Bruns A, Eckhorn R (2004) Task-related coupling from high- to low-frequency signals among visual cortical areas in human subdural recordings. Int J Psychophysiol 51:97–116.

Canolty RT, Knight RT (2010) The functional role of cross-frequency coupling. Trends Cogn Sci 14:506–515.

Canolty RT, Edwards E, Dalal SS, Soltani M, Nagarajan SS, Kirsch HE, Berger MS, Barbaro NM, Knight RT (2006) High gamma power is phase-locked to theta oscillations in human neocortex. Science 313:1626–1628.

Carrol JD, Chang J (1970) Analysis of individual differences in multidimensional scaling via an N-way generalization of "Eckart-Young" decomposition. Psychometrika 35:238–319.

Cash SS, Halgren E, Dehghani N, Rossetti AO, Thesen T, Wang C, Devinsky O, Kuzniecky R, Doyle W, Madsen JR, Bromfield E, Eross L, Halász P, Karmos G, Csercsa R, Wittner L, Ulbert I (2009) The human K-complex represents an isolated cortical down-state. Science 324:1084–1087.

Chrobak JJ, Buzsáki G (1998) Gamma oscillations in the entorhinal cortex of the freely behaving rat. J Neurosci 18:388–398.

Cohen MX (2008) Assessing transient cross-frequency coupling in EEG data. J Neurosci Methods 168:494–499.

Destexhe A, Rudolph M, Paré D (2003) The high-conductance state of neocortical neurons in vivo. Nat Rev Neurosci 4:739–751.

Fries P (2005) A mechanism for cognitive dynamics: neuronal communication through neuronal coherence. Trends Cogn Sci 9:474–480.

Gregoriou GG, Gotts SJ, Zhou H, Desimone R (2009) High-frequency, long-range coupling between prefrontal and visual cortex during attention. Science 324:1207–1210.

Haider B, McCormick DA (2009) Rapid neocortical dynamics: cellular and network mechanisms. Neuron 62:171–189.

Haider B, Duque A, Hasenstaub AR, McCormick DA (2006) Neocortical network activity *in vivo* is generated through a dynamic balance of excitation and inhibition. J Neurosci 26:4535–4545.

Haider B, Duque A, Hasenstaub AR, Yu Y, McCormick DA (2007) Enhancement of visual responsiveness by spontaneous local network activity in vivo. J Neurophysiol 97:4186–4202.

Harshman RA (1970) Foundations of the PARAFAC procedure: model and conditions for an "explanatory" multi-mode factor analysis. UCLA Work Paper Phon 16:1–84.

Hasenstaub A, Shu Y, Haider B, Kraushaar U, Duque A, McCormick DA (2005) Inhibitory postsynaptic potentials carry synchronized frequency information in active cortical networks. Neuron 47:423–435.

He BJ, Zempel JM, Snyder AZ, Raichle ME (2010) The temporal structures and functional significance of scale-free brain activity. Neuron 66:353–369.

He BJ, Snyder AZ, Zempel JM, Smyth MD, Raichle ME (2008) Electrophysiological correlates of the brain's intrinsic large-scale functional architecture. Proc Natl Acad Sci U S A 105:16039–16044.

Hô N, Destexhe A (2000) Synaptic background activity enhances the responsiveness of neocortical pyramidal neurons. J Neurophysiol 84:1488–1496.

Jacobs J, Kahana MJ (2009) Neural representations of individual stimuli in humans revealed by gamma-band electrocorticographic activity. J Neurosci 29:10203–10214.

Jensen O, Colgin LL (2007) Cross-frequency coupling between neuronal oscillations. Trends Cogn Sci 11:267–269.

Lakatos P, Shah AS, Knuth KH, Ulbert I, Karmos G, Schroeder CE (2005) An oscillatory hierarchy controlling neuronal excitability and stimulus processing in the auditory cortex. J Neurophysiol 94:1904–1911.

Lakatos P, Karmos G, Mehta AD, Ulbert I, Schroeder CE (2008) Entrainment of neuronal oscillations as a mechanism of attentional selection. Science 320:110–113.

Maris E, van Vugt M, Kahana M (2011) Spatially distributed patterns of oscillatory coupling between high-frequency amplitudes and low-frequency phases in human iEEG. Neuroimage 54:836–850.

Massimini M, Huber R, Ferrarelli F, Hill S, Tononi G (2004) The sleep slow oscillation as a traveling wave. J Neurosci 24:6862–6870.

Miller KJ, Hermes D, Honey CJ, Sharma M, Rao RP, den Nijs M, Fetz EE, Sejnowski TJ, Hebb AO, Ojemann JG, Makeig S, Leuthardt EC (2010) Dynamic modulation of local population activity by rhythm phase in human occipital cortex during a visual search task. Front Hum Neurosci 4:197.

Mormann F, Fell J, Axmacher N, Weber B, Lehnertz K, Elger CE, Fernández G (2005) Phase/amplitude reset and theta-gamma interaction in the human medial temporal lobe during a continuous word recognition memory task. Hippocampus 15:890–900.

Mørup M, Hansen LK, Herrmann CS, Parnas J, Arnfred SM (2006) Parallel factor analysis as an exploratory tool for wavelet transformed event-related EEG. Neuroimage 29:938–947.

Nowak LG, Sanchez-Vives MV, McCormick DA (1997) Influence of low and high frequency inputs on spike timing in visual cortical neurons. Cereb Cortex 7:487–501.

Oostenveld R, Fries P, Maris E, Schoffelen JM (2011) FieldTrip: open source software for advanced analysis of MEG, EEG, and invasive electrophysiological data. Comput Intell Neurosci 2011:9 pages. doi:10.1155/2011/156869.

Osipova D, Hermes D, Jensen O (2008) Gamma power is phase-locked to posterior alpha activity. PLoS One 3:e3990.

Penny WD, Duzel E, Miller KJ, Ojemann JG (2008) Testing for nested oscillation. J Neurosci Methods 174:50–61.

Raghavachari S, Lisman JE, Tully M, Madsen JR, Bromfield EB, Kahana MJ (2006) Theta oscillations in human cortex during a working-memory task: evidence for local generators. J Neurophysiol 95:1630–1638.

Rizzuto DS, Madsen JR, Bromfield EB, Schulze-Bonhage A, Seelig D, Aschenbrenner-Scheibe R, Kahana MJ (2003) Reset of human neocortical oscillations during a working memory task. Proc Natl Acad Sci U S A 100:7931–7936.

Sanchez-Vives MV, McCormick DA (2000) Cellular and network mechanisms of rhythmic recurrent activity in neocortex. Nat Neurosci 3:1027–1034.

Schack B, Vath N, Petsche H, Geissler HG, Möller E (2002) Phase-coupling of theta-gamma EEG rhythms during short-term memory processing. Int J Psychophysiol 44:143–163.

Shu Y, Hasenstaub A, Badoual M, Bal T, McCormick DA (2003) Barrages of synaptic activity control the gain and sensitivity of cortical neurons. J Neurosci 23:10388–10401.

Sidiropoulos ND, Giannakis GB, Bro R (2000) Blind PARAFAC receivers for DS-CDMA systems. IEEE Trans Signal Process 48:810–823.

Singer W (1999) Neuronal synchrony: a versatile code for the definition of relations? Neuron 24:49–65, 111–125.

Singer W, Gray CM (1995) Visual feature integration and the temporal correlation hypothesis. Annu Rev Neurosci 18:555–586.

Sirota A, Montgomery S, Fujisawa S, Isomura Y, Zugaro M, Buzsáki G (2008) Entrainment of neocortical neurons and gamma oscillations by the hippocampal theta rhythm. Neuron 60:683–697.

Steriade M, Nuñez A, Amzica F (1993) A novel slow (<1 Hz) oscillation of

neocortical neurons *in vivo*: depolarizing and hyperpolarizing components. J Neurosci 13:3252–3265.

Steriade M, Timofeev I, Grenier F (2001) Natural waking and sleep states: a view from inside neocortical neurons. J Neurophysiol 85:1969–1985.

Sternberg S (1966) High-speed scanning in human memory. Science 153:652–654.

Talairach J, Tornoux P (1988) Co-planar stereotaxic atlas of the human brain: 3-dimensional proportional system: an approach to cerebral imaging. Stuttgart, Germany: Thieme.

Tort AB, Kramer MA, Thorn C, Gibson DJ, Kubota Y, Graybiel AM, Kopell NJ (2008) Dynamic cross-frequency couplings of local field potential oscillations in rat striatum and hippocampus during performance of a T-maze task. Proc Natl Acad Sci U S A 105:20517–20522.

van Vugt MK, Schulze-Bonhage A, Litt B, Brandt A, Kahana MJ (2010) Hippocampal gamma oscillations increase with memory load. J Neurosci 30:2694–2699.

Vogels TP, Abbott LF (2009) Gating multiple signals through detailed balance of excitation and inhibition in spiking networks. Nat Neurosci 12:483–491.

Volgushev M, Chauvette S, Mukovski M, Timofeev I (2006) Precise long-range synchronization of activity and silence in neocortical neurons during slow-wave sleep. J Neurosci 26:5665–5672.

von Stein A, Sarnthein J (2000) Different frequencies for different scales of cortical integration: from local gamma to long range alpha/theta synchronization. Int J Psychophysiol 38:301–313.

Voytek B, Canolty RT, Shestyuk A, Crone N, Parvizi J, Knight RT (2010) Shifts in gamma phase-amplitude coupling frequency from theta to alpha over posterior cortex during visual tasks. Front Human Neurosci 4:191.